In-vitro degradation behavior of Mg alloy coated by fluorine doped hydroxyapatite and calcium deficient hydroxyapatite

H. R. BAKHSHESHI-RAD[1], E. HAMZAH[1], M. DAROONPARVAR[1],
M. A. M. YAJID[1], M. KASIRI-ASGARANI[2], M. R. ABDUL-KADIR[1], M. MEDRAJ[3]

1. Department of Materials, Manufacturing and Industrial Engineering, Faculty of Mechanical Engineering,
Universiti Teknologi Malaysia, 81310 Johor Bahru, Johor, Malaysia;
2. Materials Engineering Department, Najafabad Branch, Islamic Azad University, Najafabad, Isfahan, Iran;
3. Department of Mechanical Engineering, Concordia University, 1455 De Maisonneuve Blvd. West,
Montreal, QC H3G 1M8, Canada

Abstract: Fluorine-doped hydroxyapatite (FHA) and calcium deficient hydroxyapatite (CDHA) were coated on the surface of biodegradable magnesium alloy using electrochemical deposition (ED) technique. Coating characterization was investigated by X-ray diffraction (XRD), Fourier-transformed infrared spectroscopy (FTIR), transmission electron microscopy (TEM), scanning electron microscopy (SEM) and energy dispersive X-ray spectroscopy (EDS). The result shows that nano-FHA coated sample presents nano needle-like structure, which is oriented perpendicular to the surface of the substrate with denser and more uniform layers compared to the nano-CDHA coated sample. The nano-FHA coating shows smaller crystallite size (65 nm) compared to the nano-CDHA coating (95 nm); however, CDHA presents thicker layer (19 μm in thickness) compared to the nano-FHA (15 μm in thickness). The corrosion behaviour determined by polarization, immersion and hydrogen evolution tests indicates that the nano-FHA and nano-CDHA coatings significantly decrease corrosion rate and induce passivation. The nano-FHA and nano-CDHA coatings can accelerate the formation of bone-like apatite layer and significantly decrease the dissolution rate as compared to the uncoated Mg alloy. The nano-FHA coating provides effective protection to Mg alloy and presents the highest corrosion resistance. Therefore, the nano-FHA coating on Mg alloy is suggested as a great candidate for orthopaedic applications.
Key words: magnesium alloy; fluorine-doped hydroxyapatite; calcium deficient hydroxyapatite; electrodeposition; corrosion behavior

1 Introduction

Magnesium and its alloys are essential elements for the human body and are involved in many metabolic functions due to their modulate transport functions and receptors, enzyme activity, nucleic acid and protein synthesis [1,2]. Mg and its alloys also can provide good biocompatibility for orthopaedic applications, particularly as temporary stent [3−5]. However, the application of these materials has been limited due to the high corrosion rates in physiological conditions, the generation of H_2 gas and their rapid biodegradation before the new tissue has been adequately healed [6−9]. Thus, in order to improve corrosion resistance, fluorine-doped hydroxyapatite (FHA) and hydroxyapatite (HA)

coating were synthesized on the Mg alloys [1,10]. HA is calcium phosphate bioceramic material with chemical formula $[Ca_{10}(PO_4)_6(OH)_2]$ and Ca/P ratio of 1.67 [11]. HA is also the main compound of natural bone since bone contains 70% HA by mass and 50% HA by volume. Furthermore, HA shows excellent biocompatibility, bioaffinity, and osteoconductivity which make it useful in low-load bearing porous implants and for the coating of metallic implants [12,13]. HA is also the main inorganic component of bone and has been clinically and successfully used in orthopaedics and dentistry [14,15]. The order of solubility is HA $\ll$ β-TCP $<$ α-TCP $<$ DCPD, which indicates that HA is the most stable of the four materials [16]. Good HA biocompatibility and osteoconductivity cause bone cells to grow on its surface [17].

However, Mg^{+2} ions hinder the crystallization of HA. Besides, HA coating is fragile and easily broken down after long-term immersion [1]. In addition, HA shows poor mechanical properties particularly in wet environments due to its brittle behavior [18]. The biodegradation of hydroxyapatite exposed to the simulated body fluid (SBF) is the other main limitation factor because it causes the formation of unstable interface between porous or dense hydroxyapatite and bone [19,20].

In comparison with HA coating, FHA coatings could provide lower dissolution rate, lower solubility, better apatite-like layer deposition, better protein adsorption, better cell attachment and improved alkaline phosphatase activity in cell culture [21−23]. WANG et al [23] fabricated HA and FHA on titanium substrates and their results revealed that the FHA coatings showed higher bonding strength and lower dissolution rate than pure HA coating. LEE et al [24] studied the coating of calcium phosphate on titanium, and their result showed that the dissolution rate of the fluoridated coatings was lower than that of the pure HA coating. Hence, fluorine-doped hydroxyapatite ($Ca_{10}(PO_4)_6$ $(OH)_{2-x}F_x$, $0<x<2$) was developed as promising candidate for replacement of HA orthopaedic applications [25,26]. If the OH^- in HA is completely replaced via F^-, fluorapatite (FA, $Ca_{10}(PO_4)_6F_2$) is formed [25]. Although the replacement does not significantly change the crystallographic properties of HA, it has substantial effect on the mechanical properties and corrosion behaviour of HA [19]. F^- ion is a good nucleation agent for apatite [17], and doping F^- into the lattice of HA enhances lattice symmetry, thereby improving the structural stability of FA [20]. Fluoride is fundamental element in bone and tooth tissue, which can improve the crystallization and mineralization of calcium phosphate for new bone formation [26, 27]. FHA is also present in dental enamel, and owing to its high mechanical strength, FHA is used in dental applications [25]. It was reported that nano-FHA provided small amount of fluoride for improving bone formation [20]. Therefore, synthesis of FHA via different techniques such as precipitation, hydrolysis, hydrothermal, sol−gel, and mechanochemical methods receives great attentions. Among these, electrodeposition (ED) is a promising method for coating calcium phosphate on magnesium and its alloys owing to its simple set up, cost-effectiveness, ability to form uniform coating, low temperature process and ability to coat on complex shapes [27−30]. Several studies [30−33] were conducted on the synthesis and coating of HA on biodegradable magnesium based-alloys. However, doping of F^- ions into CDHA has been barely studied. Thus, the main aim of this work is to synthesize nanocrystalline FHA ($Ca_{10}(PO_4)_6F_2$) using ED process.

In addition, the microstructure and in-vitro corrosion behavior of FHA coating in comparison with that of the CDHA coating are studied to reveal the effect of doping of F^- ions into HA on the microstructure and corrosion properties.

2. Experimental

2.1 Preparation of materials

Pure magnesium (99.98%), pure zinc (99.99%) and Mg−32%Ca master alloy were used to prepare magnesium alloys. Melting was conducted in electric resistance furnace under argon gas in mild steel crucible coated with boron nitride. The melting temperature was set at 760 °C and the melt was kept for 45 min at this temperature. The melt, with concentration of 1% Ca and 3% Zn (mass fraction), was then cast into stainless steel mould pre-heated to 300 °C to produce ingot. In preparation for further experiments, several Mg−1Ca−3Zn specimens with composition of 0.054% Si, 0.032% Mn, 3.321% Zn, 1.124% Ca, 0.024% Al, 0.011% Fe and 95.434% Mg with the dimensions of 20 mm × 15 mm × 10 mm were cut from the ingot. Then, they are mechanically wet ground with 320−2000 mesh SiC grit papers until all visible scratches were removed.

2.2 Electrochemical deposition

Prior to deposition, the polished specimens were washed thoroughly with distilled water, rinsed and ultrasonically degreased with ethanol, and dried in warm stream of air. Calcium phosphate coating was produced via electrodeposition at 70 °C for 1 h. A conventional cell was fitted with graphite rod as the anode and with Mg−Ca−Zn sheet (15 mm×15 mm×10 mm) as the cathode. Saturated calomel electrode (SCE) served as reference electrode along with potentiostat/galvanostat instrument (VersaSTAT 3–VersaStudio software) for electrochemical measurements. The current density was adjusted to 0.4 mA/cm^2 for coating of the DCPD and FHA onto the specimen. The solution concentration was kept uniform using magnetic stirrer controlled at 120 r/min. The electrolyte was prepared by dissolution of 0.042 mol/L $Ca(NO_3)_2$, 0.025 mol/L $NH_4H_2PO_4$, 0.1 mol/L $NaNO_3$ and 10 mol/L H_2O_2. The addition of $NaNO_3$ led to enhancement of the ionic strength. All of the aforementioned reagents were analytically graded. The pH value of the solution was adjusted to 5.0 by adding HNO_3 and $(CH_2OH)_3CNH_2$ at room temperature. Alkaline treatment was carried out on the DCPD coating specimens to attain CDHA coating via the immersion of DCPD coated specimens into the 0.1 mol/L NaOH solution at 70 °C for 2 h. After immersion, the samples were rinsed with distilled water and subsequently dried. The FHA coating was directly electrodeposited by

adding 0.1 mol/L $NaNO_3$ and 2 mmol/L NaF at (60±1) °C into the electrolyte. The addition of 2 mmol/L NaF to the electrolyte ensured crystallized apatite structure in the FHA coating.

2.3 Characterization of coat

X-ray diffractometer (Siemens−D5000) was used to evaluate the phase transformation and crystallite size using Cu K$_\alpha$ radiation (λ=1.5405 Å) generated at 35 kV and 25 mA. The crystallite size was determined by the Scherer equation [13,27] as follows:

$$\beta=0.89\lambda/(t\cos\theta) \tag{1}$$

where β is the diffraction peak width at mid-height, λ is the X-ray wave length, t is the average crystallite size (nm), and θ is the Bragg diffraction angle.

Fourier transform infrared (FTIR) spectroscopy was used to determine the surface functional groups of the calcium phosphate coating. The FTIR spectrum was recorded in a spectral range of 4000−450 cm^{-1}.

Microstructure observation was performed using scanning electron microscope (SEM, JEOL JSM-6380LA) equipped with EDS analysis. Coating thickness was estimated by cross sectional FE-SEM observation of the FHA and CDHA coated specimens. Transmission electron microscope (TEM, Hitachi) was used to determine the size and morphology of the fine powders.

2.4 Electrochemical tests

Rectangular specimens with surface area of 1 cm^2 were molded in epoxy resin for electrochemical tests. The tests were conducted at 37 °C in open air glass cell containing 350 mL Kokubo solution at pH 7.66 using PARSTAT 2263 potentiostat/galvanostat (Princeton Applied Research). Three-electrode cell was used for potentiodynamic polarization tests, where the reference electrode was the saturated calomel electrode (SCE), the counter electrode was made of graphite rod, and the specimen was the working electrode. All experiments were carried out at a constant scan rate of 0.5 mV/s initiated at −250 mV below the open-circuit potential.

2.5 Immersion test

The immersion tests of the composite coated, fluoride treated and untreated specimens were conducted according to the ASTM G31-72 standard. The specimens were washed thoroughly with distilled water, rinsed, ultrasonically degreased with ethanol, and subsequently dried at room temperature. The specimens were then immersed in beaker containing 200 mL of Kokubo simulated body fluid (SBF) with chemical composition as listed in Table 1. The average pH value of the SBF from three measurements was recorded during the soaking experiment after 24 h intervals. After the

immersion test, the surface appearance of corroded specimens was assessed using SEM and EDS. The hydrogen evolution rate of the specimens was also measured during the 168 h immersion in Kokubo solution experiment. Two replicas were immersed in beaker where funnel was located over the samples to collect evolved hydrogen in burette above the funnel. The hydrogen evolution rate was calculated in mL·cm^{-2}·d^{-1} before renewing the solution.

Table 1 Chemical composition of Kokubo simulated body fluid (SBF) compared to human blood plasma

Solution	Ion concentration/(mmol·L^{-1})							
	Na$^+$	K$^+$	Ca^{2+}	Mg^{2+}	HCO$_3^-$	Cl$^-$	HPO$_4^{2-}$	SO$_4^{2-}$
Plasma	142.0	5.0	2.5	1.5	27.0	103.0	1.0	0.5
Kokubo (c-SBF)	142.0	5.0	2.5	1.5	4.2	147.8	1.0	0.5

3 Results and discussion

3.1 Microstructure and Composition

Figure 1 shows the XRD patterns of the CDHA and FHA coating and uncoated Mg−Ca−Zn alloy. FHA coated specimens indicate that the typical diffraction peaks at 2θ of 25.81°, 31.6°, 32.1°, 32.7°, 34° and 36.8° are accompanied by small positional shifts towards higher angles, which is due to the replacement of the F$^-$ ion (1.32 Å) for OH$^-$ group (1.68 Å) during ED process. Based on the available crystallographic data, FHA has very similar crystal structure and belongs to the same space group as HA (space group: $P63/m$; parameters: $a=b=9.462$ Å and $c=6.849$ Å, $\alpha=\beta=90°$, $\gamma=120°$). The replacement of F$^-$ ion to OH$^-$ leads to contraction in the a-axis dimensions to 0.9368 nm; however, no significant change was observed in the c-axis dimension [25]. The diffraction peaks of CDHA coated specimen are at 2θ of 20.9°, 23.4°, 25.8°, 29.3°, 31.6°, 32.7°, 34.4° and 39.8° in the coated sample besides the peaks of the substrates. This diffraction peaks are further confirmed by PDF No. 82−1943. As can be seen that typical CDHA peaks are detected in the patterns and there is no any other Ca−P compound in the coating. However, in comparison with pure HA (Fig. 1(b)), CDHA coatings show the relative intensity and peak width deviating from the standard (Fig. 1(c)). The HA (PDF No. 09−432) has hexagonal system with the $P6_3/m$ space group and lattice parameters $a=9.418$ Å and $c=6.884$ Å [34]. However, the lattice constants of the CDHA were $a=9.397$ Å and $c=6.838$ Å, which can be due to small doping of Mg^{2+}, Na$^+$ and CO$_3^{2-}$ ions [2]. The substrate exhibits relatively small, although discernible reflections of Ca$_2$Mg$_6$Zn$_3$ phase with Mg reflections. The Ca$_2$Mg$_6$Zn$_3$ phase has trigonal structure with space group $P31c$ and lattice parameters
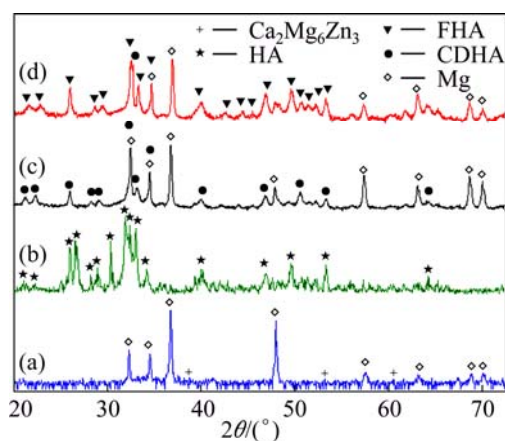
Fig. 1 XRD patterns of uncoated Mg alloy (a), pure HA (b), CDHA coated (c), and FHA coated specimen (d)

Fig. 2 FTIR characteristic bands of CDHA coated (a) and FHA coated specimen (b)

a=9.725 Å and c=10.148 Å [35].

The average crystallite size of the HA and FHA coating specimens were determined by Scherrer method. In this method, the (002) peaks are the most obvious peaks with which the average particle size of the HA and FHA coatings is calculated. The calculated crystallite size of HA coated specimens decreases from 94 to 65 nm following the replacement of OH$^-$ by F$^-$ ions which leads to the formation of FHA. It was reported that HA has skewed hexagonal molecular structure and its lattice stability declines with escalation of the molecule queue. The substitution of OH$^-$ by F$^-$ ions into the HA lattice enhances the lattice symmetry, and the FHA lattice contracts within the plane (0002), thus improving the structural stability of FHA [36].

The FTIR spectra of FHA and CDHA powder scraped from the coating specimens are shown in Fig. 2. It can be seen that the absorption band at 1641 cm^{-1} is due to O—H stretching vibration which indicates the presence of water molecules in the FHA structure. The disappearance of the bands at 3703 cm^{-1} could be due to the substitution of OH$^-$ by F$^-$ ions into the HA lattice and the formation of FHA. In addition, a significant change is that both the vibration number and the peak position change, owing to the F$^-$ ions joining the channel structure, which could be explained by location group and factor group theory model [26]. However, the absorption band at 1439 cm^{-1} is attributed to the vibration of the HCO^{-3} group. Numerous water molecules exist between the individual Ca$_9$(PO$_4$)$_6$ clusters in the spherical structure of the amorphous precursor [34]. These peaks exhibit that FHA contained some CO$_3^{-2}$ groups in PO$_4^{3-}$ sites of apatite lattice (β-type substitution). Since carbonates are constituents of hard tissue structures, the presence of low CO$_3^{-2}$ content can improve the bioactivity of FHA [37]. The absence of OH$^-$ band at 630 cm^{-1} and the appearance of the band at
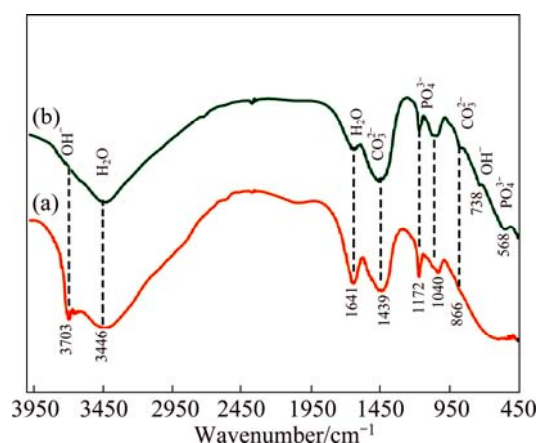
738 cm^{-1} correspond to the shifting of OH$^-$ liberation mode which indicates complete transformation of HA into FHA. It was reported that nano-FHA with high fluorine content is appropriate for dental applications as these compounds are less soluble in acidic conditions [25]. There are four types of OH$^-$ absorption bands: first, the "normal" OH$^-$ in an extended OH$^-$ chain in the form of ···OHOHOH···; second, "tail to tail" in the form of HO:OH; third, the F$^-$ bonds OH$^-$ in the symmetrical band in the form of ···OHFHO···; and finally, F$^-$ rich chains containing only a few OH$^-$ which F$^-$ bonds OH$^-$ in the symmetrical band in the form of ···FFOHFF··· [38]. The vibration bands related to PO$_4^{3-}$ ion are observed at 568 cm^{-1} (v_4), 1172 cm^{-1} (v_4) and 1040 cm^{-1} (v_3). The existence of phosphate vibrations confirms the transformation of the amorphous phase into the crystalline phase. This result is in accordance with the previous work of RÖSSLER et al [34]. However, HA coating presented a band at 1439 cm^{-1} showing the incorporation of the carbonate group into the HA lattice. PARK et al [39] reported that bone apatite contained 2% to 6% (mass fraction) of carbonate which commonly substitutes for PO$_4^{3-}$and had relatively low crystallinity since CO$_3^{2-}$ disturbs crystallization. Furthermore, carbonate can be formed by the reaction of hydroxyl ions (OH$^-$) with carbon dioxide attained from the air within the drying process. The OH$^-$ stretching vibration band is observed at 3703 cm^{-1}, showing the existence of water molecules in the HA structure.

The SEM images of uncoated, CDHA and FHA coated samples show that the Mg−1Ca−3Zn microstructure consists of α-Mg and Ca$_2$Mg$_6$Zn$_3$ phases which leads to the formation of (α-Mg+Ca$_2$Mg$_6$Zn$_3$) along the grain boundaries (Fig. 3(a)). The corresponding EDS analysis suggests that the lamellar area, which is composed of Mg, Ca and Zn, is related to the evolution of eutectic phase. The SEM images of CDHA and FHA
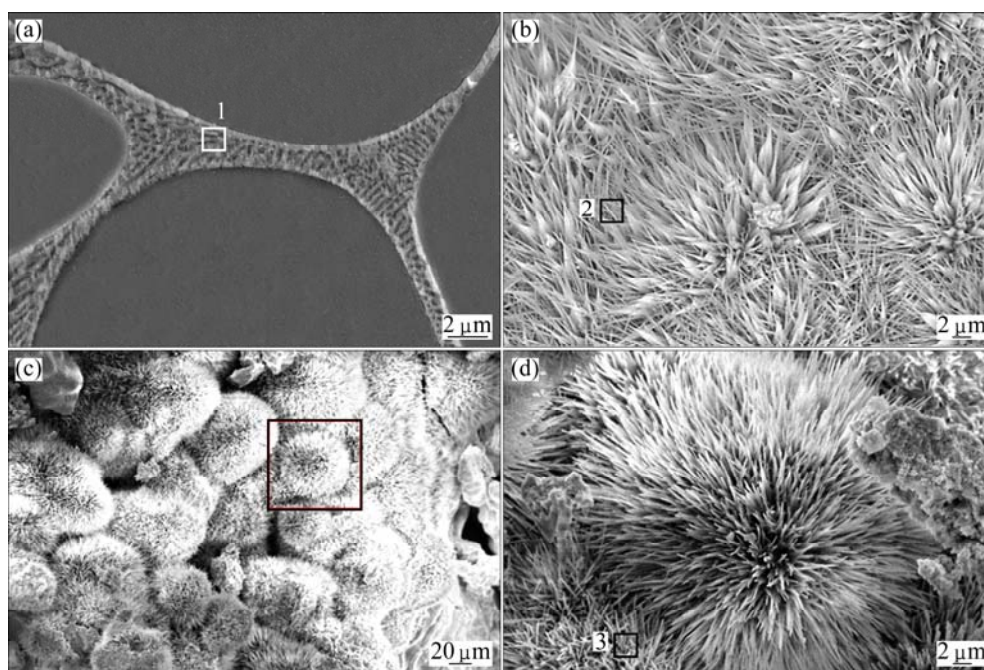
Fig. 3 SEM images of surface of uncoated Mg−1Ca−3Zn alloy (a), CDHA coated (b) and FHA coated specimen (c, d)

coatings show that calcium phosphate coated specimen consisting of petal-like structure accumulated on the surface of the substrate (Figs. 3(c) and (d)). The FHA has nano-scaled apatite crystals with very fine needle-like shape and nano-pores formed between those nano-crystals. The FHA crystallites is small in diameter, less than 60−75 nm, which is very close to the HA crystals in mature human dental enamel. In this case, it was reported that materials with similar crystal structure, size and morphology to bone mineral can enhance the bioactivity and osteoconductivity of the coating [26]. These bioceramic films were synthesized to assist in the generation of new bone on dental or orthopaedic implanted prosthesis. However, CDHA coating displays stacked flower-pattern with almost uniform and upright structure distributed uniformly on the surface of the substrate. The needle-like morphology has greater surface area than the plate-like morphology for the deposition of Ca, P in the SBF solution. The EDS analysis of HA coated specimens reveals that the coating layers consist of magnesium, calcium, oxygen, carbon and trace amounts of zinc which originate from the substrate (Fig. 4(b)). The presence of carbon in the coating is due to the dissolution of CO_2 in the atmosphere. The Ca/P mole ratio of HA is about 1.47, indicating the formation of calcium deficient HA (CDHA). The ratio is lower than stoichiometric hydroxyapatite (1.67), indicating the formation of solid solubility [22]. DOROZHKIN [16] reported that Ca-deficient apatite formed when the Ca/P mole ratio was between 1.33 and 1.55. This Ca-deficient coating is more soluble and may induce the precipitation of new

bonelike apatite rapidly after implantation [21,22,28,35]. The EDS analysis of FHA coated specimens reveals that the coating layers consist of magnesium, calcium, oxygen, carbon and trace amount of fluoride elements (Fig. 4(c)). The presence of fluorine shows that the substitution of OH$^-$ by F$^-$ ions occurs during the coating process which is beneficial to the mineralization and crystallization of calcium phosphate in the new bone forming process [21]. Fluorine plays a fundamental role in influencing the physical and biological properties of the deposition film [21,40]. The Ca/P mole ratio of FHA is about 1.41 which is lower than the theoretical value (1.67). This indicates that calcium deficient FHA deposits on the substrate. It was reported [21] that FHA coatings were calcium deficient where Mg^{2+} and Na^+ ions substituted Ca^{2+}. The calcium deficient apatite can promote the formation of new bone in-vivo. The existence of Na^+, Mg^{2+} and F$^-$ can also improve the bioactivity of FHA coatings because the composition of fluorine-doped hydroxyapatite is similar to the natural bone minerals [21].

Figure 5 shows the TEM images and related selected area electron diffraction (SAED) pattern of the FHA and CDHA coatings. It is found that the needle-like particles formed in the coatings are about 65 nm in diameter. The lattice spacings of (002) HA and (120) HA are estimated to be 0.34 and 0.47 nm, respectively, as shown in Fig. 5(c). These values are consistent with the calculated values (0.344 nm for (002) HA and 0.471 nm for (120) HA) using the lattice parameters of a=9.421 Å, b=9.421 Å, c=6.882 Å, α=90°, β=90° and γ=120° [41]. The sharp diffraction peaks of HA phase (Fig. 5(c))
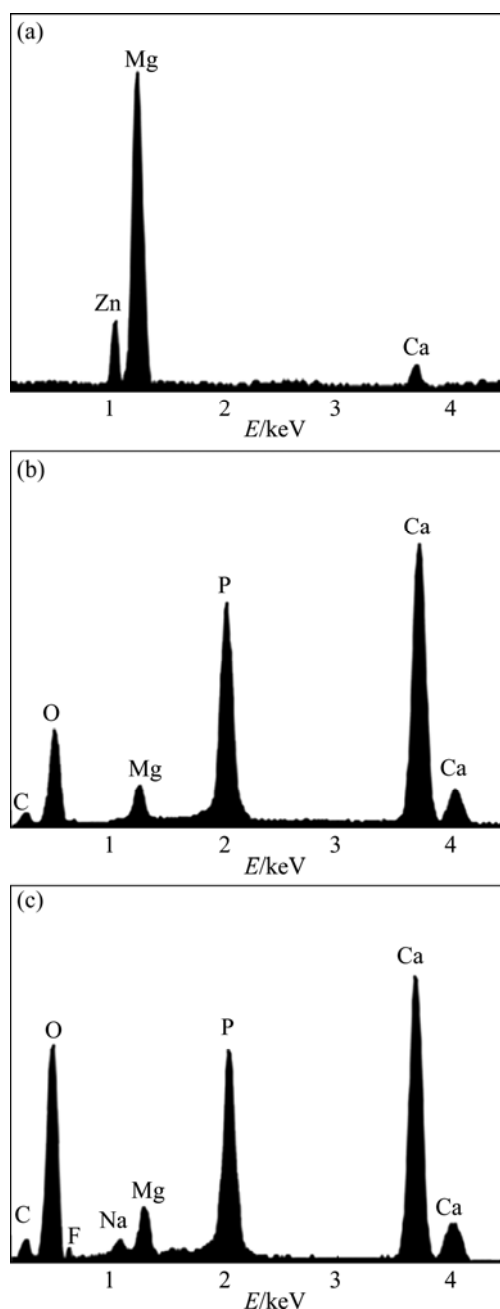
Fig. 4 EDS analysis of uncoated, CDHA and FHA coatings in Fig. 3: (a) Region 1; (b) Region 2; (c) Region 3

demonstrate that the single crystal of needle-like HA is highly crystallized. It is obvious that FHA coated sample is composed of finer needle-like particles compared to the CDHA coated sample (Fig. 5(b)).

　　Figure 6 shows the cross sections of the CDHA and FHA coatings with thicknesses of 19 and 15 μm, respectively. Cross sections of the coatings appear to be very dense and relatively uniform in thickness. However, there are some micro pores and micro flaws in the film, but they are not entirely transverse in the coatings. Therefore, the substrates are covered by protective layer, which consists of relatively thermodynamically stable
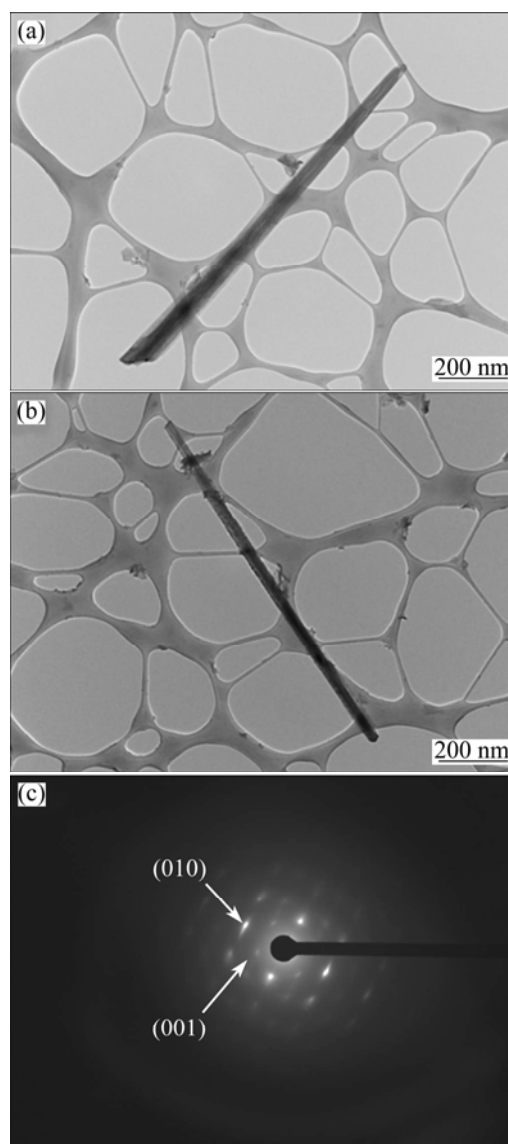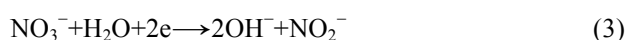

Fig. 5 TEM images of CDHA coating (a), FHA coating (b) and SAED pattern of CDHA coating (c)

compounds. The presence of CDHA and FHA film, which acts as protective layer on the surface of the sample, is the main reason of the corrosion rate reduction. The protective layer blocks the reaction for species transportation (such as water and chlorine), hence increasing the corrosion resistance of the sample.

　　The mechanism of electrolytic deposition can be described as a series of electrochemical reactions. The three possible sources of OH$^-$ at the cathode [22,26] are as follows:

$$O_2+2H_2O+4e\longrightarrow 4OH^- \qquad (2)$$

$$NO_3^-+H_2O+2e\longrightarrow 2OH^-+NO_2^- \qquad (3)$$

$$2H_2O+2e\longrightarrow H_2+2OH^- \qquad (4)$$

　　Hydroxide ions fabricated during the electrodeposition process results in an increase of the pH
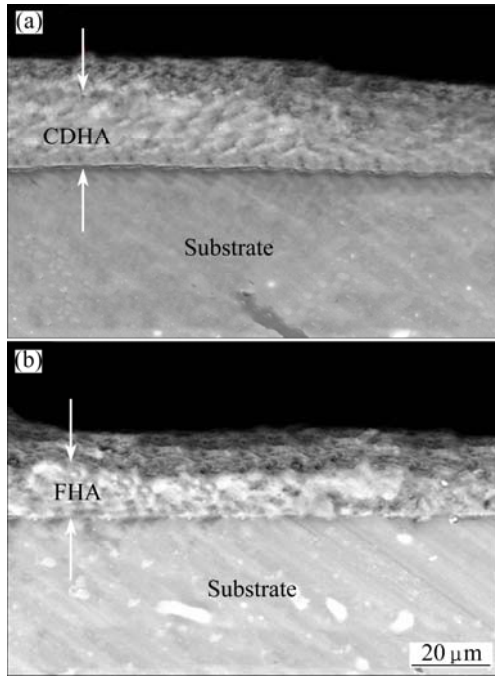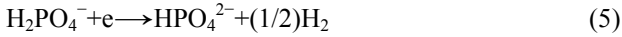
Fig. 6 Cross-sectional SEM images of CDHA coating (a) and FHA coating (b)

in the vicinity of the cathode, which results in the following reactions:

$$H_2PO_4^- + e \longrightarrow HPO_4^{2-} + (1/2)H_2 \qquad (5)$$

$$H_2PO_4^- + 2e \longrightarrow PO_4^{3-} + H_2 \qquad (6)$$

$$H_2PO_4^- \longrightarrow HPO_4^{2-} + H^+ \qquad (7)$$

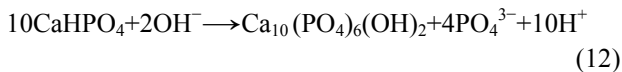$$HPO_4^{2-} \longrightarrow PO_4^{3-} + H^+ \qquad (8)$$

The precipitation of phosphate ions occurs due to the acid-base reactions which are vital for crystallization process formation of FHA coating film according to the following reactions:
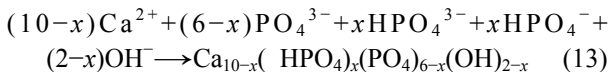
$$H_2PO_4^- + OH^- \longrightarrow HPO_4^{2-} + H_2O \qquad (9)$$

$$H_2PO_4^- + H_2O + 2e \longrightarrow H_2PO_3^- + 2OH^- \qquad (10)$$
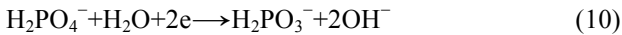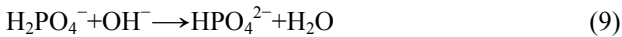
The suitable local chemical environment in the vicinity of the cathode enables the HPO_4^{2-} to combine with Ca^{2+} to produce dicalcium phosphate dihydrate which precipitates on the surface of the substrate through the following reaction [23,42]:

$$Ca^{2+} + HPO_4^{2-} + H_2O \longrightarrow CaHPO_4 2H_2O \qquad (11)$$

The DCPD coating after alkaline treatment converts to HA according to the following reaction:

$$10CaHPO_4 + 2OH^- \longrightarrow Ca_{10}(PO_4)_6(OH)_2 + 4PO_4^{3-} + 10H^+ \qquad (12)$$

The CDHA is formed as follows [42,43]:

$$(10-x)Ca^{2+} + (6-x)PO_4^{3-} + xHPO_4^{3-} + xHPO_4^- + (2-x)OH^- \longrightarrow Ca_{10-x}(HPO_4)_x(PO_4)_{6-x}(OH)_{2-x} \qquad (13)$$

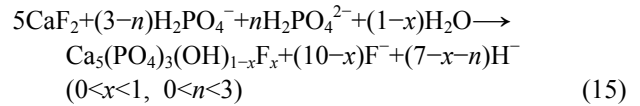where $0 < x \leq 2$.

The addition of NaF into the electrolyte leads to the occurrence of the following reactions. In this case, at first, Ca^{2+} ions rapidly consume F^- ions in the electrolyte to form CaF_2 which can be expressed as follows [42,43]:

$$Ca_5(PO_4)_3OH + 10F^- + (7-n)H^+ \longrightarrow$$
$$5CaF_2 + H_2O + (3-n)H_2PO_4^- + nH_2PO_4^{2-} \qquad (14)$$
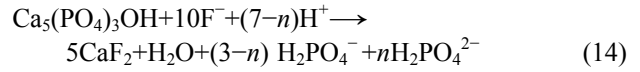
Afterward, CaF_2 particles further react with HPO_4^{2-} in the solution to deposit FHA [42,43]:

$$5CaF_2 + (3-n)H_2PO_4^- + nH_2PO_4^{2-} + (1-x)H_2O \longrightarrow$$
$$Ca_5(PO_4)_3(OH)_{1-x}F_x + (10-x)F^- + (7-x-n)H^-$$
$$(0 < x < 1, \ 0 < n < 3) \qquad (15)$$

Combining reactions (14) and (15) results in the formation of FHA via the following reaction:

$$10Ca^{2+} + 6PO_4^{3-} + xF^- + (2-x)OH^- \longrightarrow Ca_{10}(PO_4)_6F_x(OH)_{2-x}$$
$$(16)$$
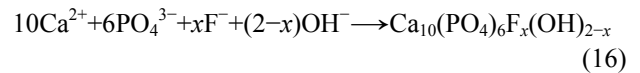
The bonding of F−H with adjacent OH^- along the c-axis can occur as the F^- ions are doped; the orientation of O—H in FHA crystals is then increased and vertical FHA crystals are produced. This has been observed in both XRD and FTIR measurements.

3.2 Electrochemical measurement

Figure 7 shows the polarization curves recorded after 1 h exposure to Kokubo solution for FHA, CDHA coated samples and uncoated Mg−Ca−Zn alloy. As can be seen that the uncoated Mg−Ca−Zn alloy has more negative corrosion potential compared to the calcium-phosphate coated specimens, indicating the role of protective layer on the corrosion behaviour of the alloy. The corrosion potential of as-cast Mg−Ca−Zn is −1726.5 mV (vs SCE) which is 122.2 mV and 160.3 mV lower than that of the FHA and HA coated samples, respectively. Obviously, the coatings enhance the protection ability of the substrates, acting as blocking layers against ion diffusion. The FHA and CDHA coatings reduce the specific surface area due to the formation of much denser film. This layer can effectively
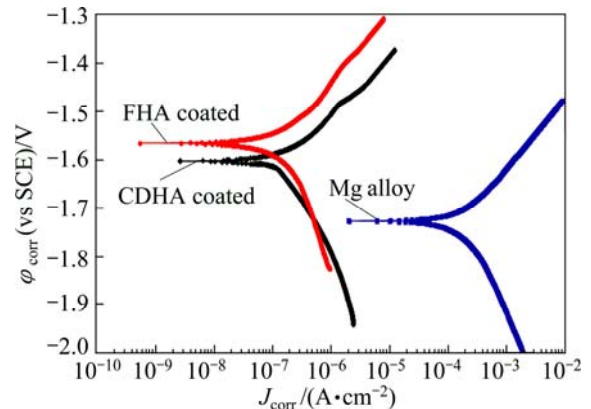

Fig. 7 Potentiodynamic polarization curves of uncoated alloys, CDHA and FHA coated samples in Kokubo solution

prevent ionic diffusion and provide corrosion protection for the Mg substrate. The corrosion current density of the FHA and CDHA coated specimens was 6.01 and 5.52 μA/cm², respectively, which is significantly lower than that of the untreated sample (295.3 μA/cm²). This is due to the formation of the protective layer which blocks the reaction for ion transportation, hence increasing the corrosion resistance of the coating samples [43,44]. In addition, it can be seen that the corrosion current density of the FHA coated sample is slightly lower compared to the CDHA coated sample in the Kokubo solution. This could be due to the fact that FHA provides much uniform and dense coating layer compared with the CDHA coated specimen.

The corrosion current density (J_{corr}), corrosion potential (φ_{corr}), cathodic Tefal slopes (β_c), anodic Tefal slopes (β_a) and corresponding corrosion rate (P_i) of specimens extracted from the polarization curves are shown in Table 2. J_{corr} is related to the P_i according to the following equation [6,45]:

$$P_i = 22.85 J_{corr} \tag{17}$$

According to Eq. (17) the corrosion rate of the uncoated Mg−Zn−Ca alloy is 6.74 mm/a. However, FHA (0.14 mm/a) and CDHA (0.13 mm/a) coated specimens show lower corrosion rate compared to the uncoated alloy. FHA films can be considered to possess good corrosion resistance, which arise from the formation of intensive microstructures when fluorine ions are introduced into the Ca−P crystal structure. As can be seen that the corrosion rate of FHA is also lower than that of the CDHA coating. This can be attributed to the FHA having better microstructures than HA coating, which can effectively protect Mg alloy substrates from corrosion in SBF. Also the polarization resistance (R_P) is calculated from the electrochemical parameters (J_{corr}, β_a and β_c) of specimens according to the following equation [27,44]:

$$R_P = \frac{\beta_a \beta_c}{2.3(\beta_a + \beta_c) J_{corr}} \tag{18}$$

The corrosion behavior of the alloy improves because R_P values increase after FHA and HA coating. The polarization resistances of FHA and CDHA coatings are 4.61 and 3.55 kΩ·cm², respectively, which are significantly higher than that of the uncoated alloy

(0.99 kΩ·cm²). The cathodic Tafel slope of FHA and CDHA coated specimens exhibits marginal difference, indicating that similar electrochemical reactions have taken place. However, the uncoated Mg alloy shows lower cathodic Tafel slope. In addition, Table 2 shows that the alloys have larger cathodic Tafel slope compared to the anodic Tafel slopes. A long passivation stage in the polarization curve of FHA and CDHA coated sample are observed whilst no passivation stage in the curve of uncoated Mg alloy can be detected. This is because the addition of FA nano particles decreases the cathodic current density, reducing the rate of hydrogen generation. The presence of passivation-like regions also indicates the formation of barrier film on the substrate surface which has considerable effect on the corrosion rate of the alloy.

3.3 Immersion test

Figure 8 shows the variation of pH values as a function of immersion duration for CDHA and FHA coated specimens accompanied by uncoated alloys in SBF for 168 h. The uncoated Mg alloy shows higher pH increase compared to the Ca−P coating, indicating higher corrosion rate the uncoated alloy. Furthermore, it can be seen that the pH values of the solution for the uncoated and the Ca−P coated samples increase with different slopes by increasing immersion duration in the initial soaking stage. The release of OH⁻ is due to the dissolution of the coating caused by rapid increase of pH value in the initial stage of immersion test [21]. However, the pH value becomes stabilized over longer immersion times. This may be due to the penetration of the solution at the interface between Ca−P coating and substrate via the pores and cracks of the coating corroded by SBF solution. The precipitation of apatite which consumes OH⁻ ions can be the other reason for the minimal pH increase at the final stage [46].

It is noted that CDHA coating shows higher pH increase than FHA coating. This can be due to the replacement of OH⁻ with F⁻ ions in the apatite structure, leading to significant reduction in the apatite dissolution rate in the SBF. It was reported that the hydrogen (H⁺) ions of HA were arranged in the atomic interstices neighboring to the oxygen ions (O^{2-}) along the *c*-axis of apatite structure, forming OH⁻ groups and were oriented

Table 2 Electrochemical parameters of uncoated alloys, CDHA and FHA coatings in Kokubo solution acquired from polarization test

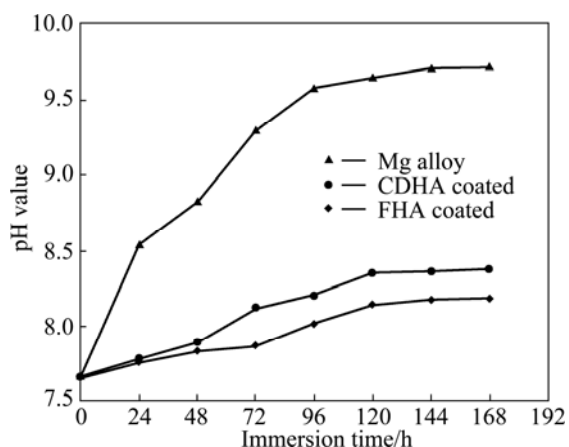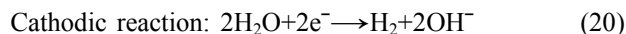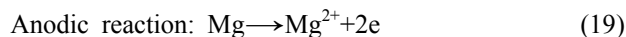| Alloy	φ_{corr} (vs SCE)/ mV	J_{corr}/ (μA·cm⁻²)	β_C (vs SCE)/ (mV·dec⁻¹)	β_a (vs SCE)/ (mV·dec⁻¹)	R_P/ (kΩ·cm²)	P_i/ (mm·a⁻¹)
Mg−1Ca−3Zn	−1726.5	295.3	298	87	0.99	6.74
CDHA coating	−1603.8	6.01	354	57	3.55	0.14
FHA coating	−1565.7	5.52	387	69	4.61	0.13

Fig. 8 Change in pH of Kokubo solution during immersion of uncoated Mg alloy, CDHA and FHA coated samples for 168 h

randomly, which resulted in a certain degree of disorder to the crystal structure of HA [38]. Once the OH^- groups were partially substituted by the F^- ions, the existing hydrogen ions of the OH^- groups were bound to the nearby F^- ions because of the higher affinity of F^- ions compared to oxygen ions, producing a quite well-ordered apatite structure, which caused an increase in chemical stability and a decrease in solubility of HA matrix. Therefore, when F^- ions were substituted for the OH^- groups in the HA matrix, a certain level of solubility resistance of the apatite ceramics was achieved [38].

The surface morphologies of FHA, CDHA and uncoated specimens immersed in SBF for 168 h are

shown in Fig. 9. The entire surface of untreated sample is covered by insoluble corrosion film of brucite $Mg(OH)_2$ and some white particles (Fig. 9(a)). When Mg based alloy specimens are exposed to the SBF solution, Mg element dissolves, and a corrosion layer is deposited according to the following reactions:

Anodic reaction: $Mg \longrightarrow Mg^{2+} + 2e$　　　　(19)

Cathodic reaction: $2H_2O + 2e^- \longrightarrow H_2 + 2OH^-$　　(20)

$Mg^{2+} + 2OH^- \longrightarrow Mg(OH)_2$　　　　　(21)

$Mg^{2+} + 2Cl^- \longrightarrow MgCl_2$　　　　　　(22)

The Mg transforms to stable Mg^{2+} ion as a result of dissolution of Mg (Reaction (19)), and the cathodic reaction occurs at the same time due to the occurrence of galvanic corrosion accompanied by hydrogen evolution (Reaction (20)). Further anodic reaction results in more Mg^{2+} dissolution in the SBF with more consumption of HCO_3^- and HPO_4^{2-}, causing an increase in the Cl^- concentration in the solution. Due to the formation of thin heterogeneous porous layer of $Mg(OH)_2$, the corrosion rate of the specimens decreases. However, the presence of aggressive Cl^- in the solution transforms $Mg(OH)_2$ into more soluble $MgCl_2$. The $MgCl_2$ then dissolves into Mg^{2+} and $2Cl^-$, causing increase in hydroxide (OH^-) ions near the surface of the sample, which leads to increase in pH of the solution. Breakdown of $Mg(OH)_2$ decreases the protected area, consequently, promoting further dissolution of the substrate. As the reaction progressed, high amounts of Mg^{2+} dissolves and
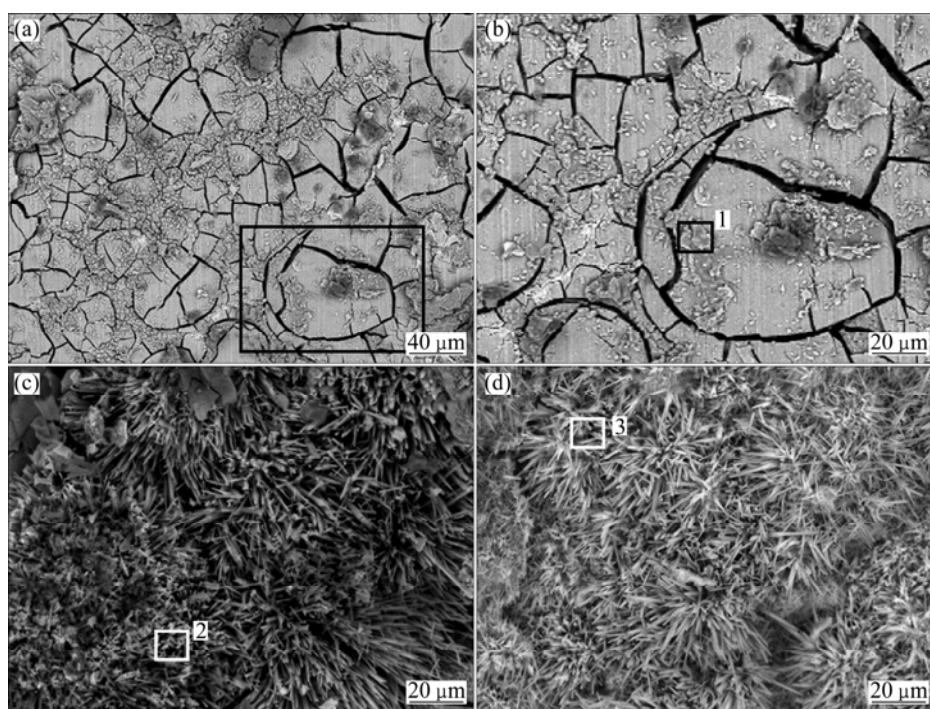

Fig. 9 SEM images of uncoated Mg alloy (a,b), CDHA coated (c) and FHA coated (d) samples after immersion into Kokubo for 168 h

subsequently, phosphate ions (HPO_4^{2-} or PO_4^{3-}) and Ca^{2+} in the solution react with OH^- to form HA. With prolonged immersion duration, additional precipitates are deposited, which causes the pores to fill, thus reducing the porosity. As the corrosion product layer becomes thicker, the amount of porosity decreases continually, which prevents the samples from further corrosion in SBF. However, it is assumed that the corrosion protection becomes weaker after longer immersion due to the existence of micropores [47]. CDHA coating presents coarse needle like morphology (rosette pattern), which covers almost the entire surface of Mg−Ca−Zn alloy (Fig. 9(c)). The EDS analysis of the corrosion product of CDHA demonstrates that the Ca/P molar ratio of the CDHA coating is higher compared to the FHA coating, indicating that more carbonate and phosphate ions can be absorbed by the CDHA coating (Figs. 10(b) and (c)).

This phenomenon presents the better bioactivity and osteoconductivity of FHA as compared to HA coating. The FHA layer with needle-like apatite crystals formed compactly and uniformly on the substrate, and nano-pores form between those nano-crystals (>100 nm) (Fig. 9(d)). The substitution of F^- ions significantly increases coating density and leads to reduction in the amount of porosity compared to the CDHA coating. The amount of precipitation declines and the size of the needle aggregates decreases due to the existence of F^- ions in the composition of the electrolyte solution. However, the higher solubility of CDHA coating sample leads to escalation of the super-saturation of the SBF solutions and start to precipitate, as in non-equilibrium conditions, the Ca^{2+} and PO_4^{3-} ions which exist in the solution are inclined to easily penetrate the solid/liquid interface, thus reducing its free energy at higher super-saturation state of SBF [38]. The EDS analysis of the corrosion product of FHA coating reveals the presence of F, Mg, Ca, P, and O elements. The Ca/P molar ratio of the compounds is 1.47.

X-ray diffraction patterns of the corrosion product from coated and uncoated specimens, as shown in Fig. 11, show that the main corrosion products formed after 168 h of exposure to SBF are $Mg(OH)_2$, HA and FHA. The resulting precipitated Ca−P on the surface of the coated alloy delays the penetration rate of the solution via the coating layer defects. Therefore, the corrosion rate of the substrate declines as a result of high thermodynamic and structural stability of Ca−P and its barrier action between the SBF solution and coating layer defects. XRD pattern indicates higher intensities of the HA phase with lower intensities of $Mg(OH)_2$ phases from Ca−P coated alloy compared to the uncoated one, indicating lesser amount of $Mg(OH)_2$ corrosion product forms on the surface of Ca−P coated alloy, acceptable
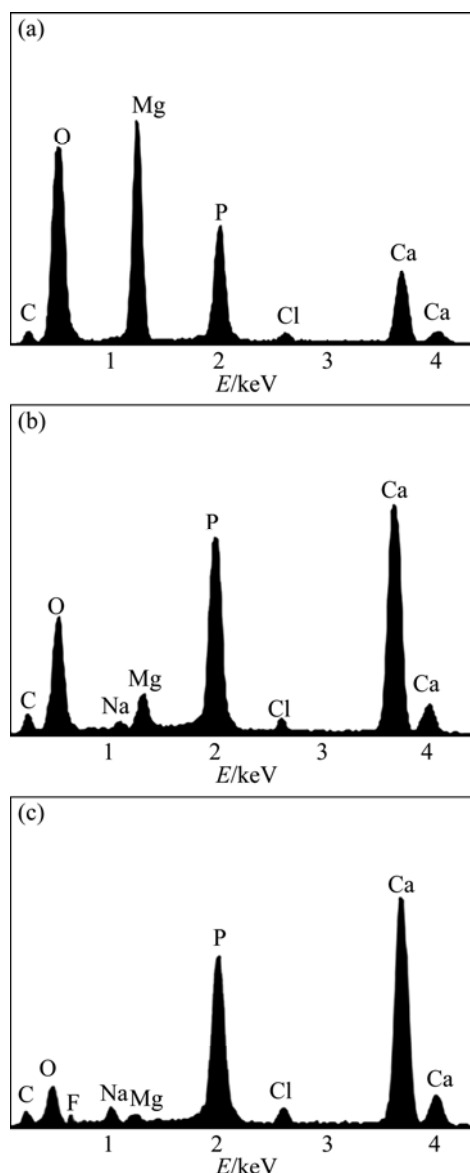

Fig. 10 EDS analysis of uncoated Mg alloy, CDHA and FHA coatings containing corrosion products from Region 1 (a), Region 2 (b), and Region 3 (c) in Fig. 9 after immersion in Kokubo solution for 168 h
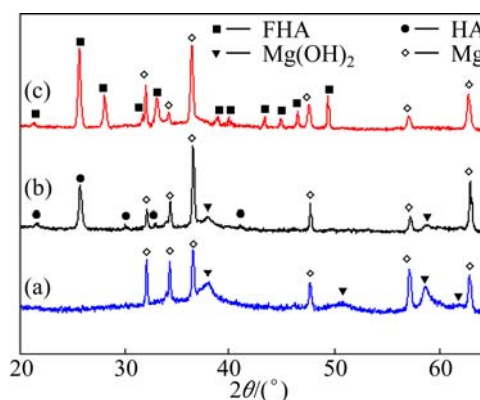

Fig. 11 XRD patterns obtained for corrosion products of uncoated alloy (a), CDHA coating (b) and FHA coating (c) after full immersion exposure to SBF solution for 168 h

result as it has lower corrosion rate than that of the uncoated one.

In comparison, the FHA coating with more dense and uniform layer before immersion acts as an effective protective layer to prevent further corrosion attack. It can be seen that no significant presence of $Mg(OH)_2$ can be detected in the corrosion products attained from FHA coating, indicating less corrosion attack occurs in FHA coated samples.

The hydrogen evolution results of the coated and uncoated specimen in Kokubo solution for 168 h are shown in Fig. 12. The FHA coated specimen shows the lowest hydrogen evolution rate of 1.11 mL·cm^{-2}·d^{-1}. The hydrogen evolution rate of the CDHA coated specimen is 1.37 mL·cm^{-2}·d^{-1}. However, the uncoated Mg alloy shows the highest hydrogen evolution rate of 5.14 mL·cm^{-2}·d^{-1}. The rate of degradation decreases since Ca−P coating can considerably hinder the degradation of the alloy. The dissolution rate of the FHA is much slower than that of the uncoated sample. Thus, it can be concluded that the FHA with doped F$^-$ ions is more chemically stable in the SBF compared to the CDHA coating, owing to their higher crystallinity and denser lattice structure [3].
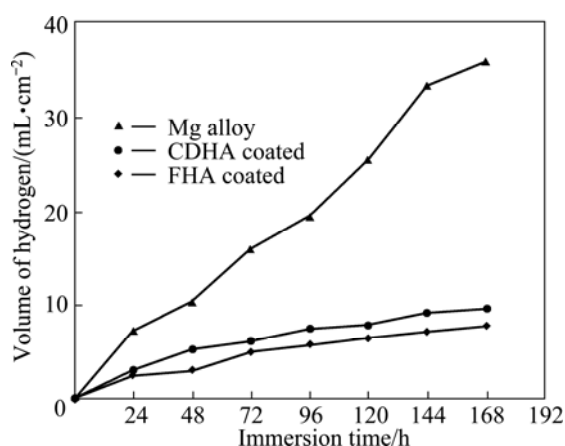

Fig. 12 Hydrogen evolution of uncoated Mg alloy, CDHA and FHA coated specimens immersed in Kokubo solution for 168 h

4 Conclusions

1) The nano-FHA and nano-CDHA coatings were prepared on the Mg−Ca−Zn alloy by ED method.

2) The nano-FHA coating provides more effective protection to the Mg alloy because it is much denser and more uniform compared to the nano-CDHA coating. The nano-FHA coating has greater surface area than the nano-CDHA coating, which enhances the nucleation site of apatite in the SBF solution.

3) The corrosion current density (J_{corr}) of the nano-FHA and nano-CDHA coated samples is 50 times lower than that of the uncoated sample. However, the nano-FHA coating shows more compact film and hence possesses a greater passivation region, which significantly slows down the corrosion rate of Mg alloy.

4) The nano-FHA and nano-CDHA coatings have considerably lower degradation rates and higher corrosion resistance compared to the uncoated Mg alloy. However, nano-FHA coating is less soluble and thus the appearance of samples remains unchanged after immersion. The results reveal that the nano-FHA coating is biodegradable with good protection to the Mg alloy, which can potentially be used for different orthopaedic implants.

References

[1]	LI J, SONG Y, ZHANG S. In vitro responses of human bone marrow stromal cells to a fluoridated hydroxyapatite coated biodegradable Mg−Zn alloy [J]. Biomaterials 2010, 31: 5782−5788.

[2]	ZHEN Z, XI T F, ZHENG Y F. A review on in vitro corrosion performance test of biodegradable metallic materials [J]. Transactions of Nonferrous Metals Society of China, 2013, 23: 2283−2293.

[3]	HUANGA Y, DINGA Q, PANGA X, HANA S, YANA Y. Corrosion behavior and biocompatibility of strontium and fluorine co-doped electrodeposited hydroxyapatite coatings [J]. Appl Surf Sci, 2013, 282: 456−462.

[4]	TAN L L, WANG Q, GENG F, XI X S, QIU J H, YANG K. Preparation and characterization of Ca−P coating on AZ31 magnesium alloy [J]. Transactions of Nonferrous Metals Society of China, 2010, 20(S2): s648−s654.

[5]	ZHANG C Y, ZENG R C, CHEN R S, LIU C L, GAO J C. Preparation of calcium phosphate coatings on Mg−1.0Ca alloy [J]. Transactions of Nonferrous Metals Soceity of China, 2010, 20(S2): s655−s659.

[6]	BAKHSHESHI-RAD H R, IDRIS M H, ABDUL-KADIR M R, OURDJINI A, MEDRAJ M, HAMZAH E. Mechanical and bio-corrosion properties of quaternary Mg–Ca–Mn–Zn alloys compared with binary Mg–Ca alloys [J]. Mater Design, 2014, 53: 283−292.

[7]	XU L P, ZHANG E L, YANG K. Biocorrosion property and cytocompatibility of calcium phosphate coated Mg alloy [J]. Transactions of Nonferrous Metals Society of China, 2012, 22: 2014−2020.

[8]	YE C H, XI T F, ZHENG Y F, WANG S Q, LI Y D. In vitro corrosion and biocompatibility of phosphating modified WE43 magnesium alloy [J]. Transactions of Nonferrous Metals Society of China, 2013, 23: 996−1001.

[9]	GUPTA R K, MENSAH-DARKWA K, SANKAR J, KUMAR D. Enhanced corrosion resistance of phytic acid coated magnesium by stearic acid treatment [J]. Transactions of Nonferrous Metals Society of China, 2013, 23: 1237−1244.

[10]	LIU G Y, TANG S W, WANG C, HU J, LI D C. Formation characteristic of Ca−P coatings on magnesium alloy surface [J]. Transactions of Nonferrous Metals Society of China, 2013, 23: 2294−2299.

[11]	JIAO M J, WANG X X. Electrolytic deposition of magnesium-substituted hydroxyapatite crystals on titanium substrate [J]. Mater Lett, 2009, 63: 2286−2289.

[12]	JAVIDI M, JAVADPOUR S, BAHROLOLOOM M E. Electrophoretic deposition of natural hydroxyapatite on medical grade 316L stainless steel [J]. Mater Sci Eng C, 2008, 28: 1509−1515.

[13] ABDEL-AAL E A, DIETRICH D, STEINHAEUSER S, WIELAGE B. Electrocrystallization of nanocrystallite calcium phosphate coatings on titanium substrate at different current densities [J]. Surf Coat Technol, 2008, 202: 5895−5900.

[14] ERGUN C, WEBSTER T, BIZIOS R. Hydroxylapatite with substituted magnesium, zinc, cadmium, and yttrium. I. Structure and microstructure [J]. J Biomed Mater Res, 2002, 59: 305−311.

[15] GENG F, TAN L L, JIN X X. The preparation, cytocompatibility, and in vitro biodegradation study of pure β-TCP on magnesium [J]. J Mater Sci: Mater Med, 2009, 20: 1149−1157.

[16] DOROZHKIN S V. Calcium orthophosphates as bioceramics: State of the Art [J]. Funct Biomater, 2010, 1: 22−107.

[17] JAMESH M, KUMAR S, SANKARA NARAYANAN T S N. Corrosion behavior of commercially pure Mg and ZM21 Mg alloy in Ringer's solution—Long term evaluation by EIS [J]. Corros Sci, 2011, 53: 645−654.

[18] DUTA L, OKTAR F N, STANE G E, POPESCU-PELIN G, SERBAN N, LUCULESCU C, MIHAILESCU I N. Novel doped hydroxyapatite thin films obtained by pulsed laser deposition [J]. Appl Surf Sci, 2013, 265: 41−49.

[19] CAI Y, ZHANG S, ZENG X, QIAN M, SUN D, WENG W. Interfacial study of magnesium-containing fluoridated hydroxyapatite coatings [J]. Thin Solid Films, 2011, 519: 4629−4633.

[20] RAZAVI M, FATHI M H, MERATIAN M. Microstructure, mechanical properties and bio-corrosion evaluation of biodegradable AZ91-FA nanocomposites for biomedical applications [J]. Mater Sci Eng A, 2010, 527: 6938−6944.

[21] MENG E C, GUAN S K, WANG H X., WANG L G. Effect of electrodeposition modes on surface characteristics and corrosion properties of fluorine-doped hydroxyapatite coatings on Mg−Zn−Ca alloy [J]. Appl Surf Sci, 2011, 257: 4811−4816.

[22] BIRA F, KHIREDDINEA H, TOUATIB A, SIDANEA D, YALAA S, OUDADESSE H. Electrochemical depositions of fluorohydroxyapatite doped by Cu^{2+}, Zn^{2+}, Ag^+ on stainless steel substrates [J]. Appl Surf Sci, 2012, 258: 7021−7030.

[23] WANG J, CHAO Y, WAN Q, ZHU Z, YU H. Fluoridated hydroxyapatite coatings on titanium obtained by electrochemical deposition [J]. Acta Biomater, 2009, 5: 1798−1807.

[24] LEE E J, LEE S H, KIM H W, KONG Y M, KIM H E. Fluoridated apatite coatings on titanium obtained by electron-beam deposition [J]. Biomaterials, 2005, 26: 3843−3851.

[25] KAHRIZSANGI R E, TABRIZI B N, CHAMI A. Characterization of single-crystal fluorapatite nanoparticles synthesized via mechanochemical method [J]. Particuology, 2011, 9: 537−544.

[26] HUANG Y, YAN Y, PANG X. Electrolytic deposition of fluorine-doped hydroxyapatite/ZrO_2 films on titanium for biomedical applications [J]. Ceram Int, 2013, 39: 245−253.

[27] BAKHSHESHI-RAD H R, IDRIS M H, ABDUL-KADIR M R. Synthesis and in vitro degradation evaluation of the nano-HA/MgF_2 and DCPD/MgF_2 composite coating on biodegradable Mg−Ca−Zn alloy [J]. Surf Coat Technol, 2013, 222: 79−89.

[28] WEN C, PENG L, REN C, WANG X, HU Z. Characterization and degradation behavior of AZ31 alloy surface modified by bone-like hydroxyapatite for implant applications [J]. Appl Surf Sci, 2009, 225: 6433−6438.

[29] HORNBERGER H, VIRTANEN S, BOCCACCINI A R. Biomedical coatings on magnesium alloys—A review [J]. Acta Biomater, 2012, 8: 2442−2455.

[30] SHADNBAZ S, DIAS G J. Calcium phosphate coatings on magnesium alloys for biomedical applications: A review [J]. Acta Biomater, 2012, 8: 20−30.

[31] SONG Y W, SHAN D Y, HAN E H. Electrodeposition of hydroxyapatite coating on AZ91D magnesium alloy for biomaterial application [J]. Mater Lett, 2008, 62: 3276−3279.

[32] WANGA H, SHAOKANG G, YISHENG W. In vivo degradation behavior of Ca-deficient hydroxyapatite coated Mg−Zn−Ca alloy for bone implant application [J]. Colloids Surfaces B, 2011, 88: 254−259.

[33] SONG Y, WANG H X, GUAN S K, WANG X. In vitro degradation and mechanical integrity of Mg−Zn−Ca alloy coated with Ca-deficient hydroxyapatite by the pulse electrodeposition process [J]. Acta Biomater, 2010, 6: 1743−1748.

[34] ROSSLER S, SEWLING A, STOLZEL M, BORN R. Electrochemically assisted deposition of thin calcium phosphate coatings at near-physiological pH and temperature [J]. J Biomed Mater Res A, 2003, 64: 655−663.

[35] BAMBERGER M, LEVI G, SANDE J B. Precipitation hardening in Mg−Ca−Zn alloys [J]. Metall Mater Trans A, 2006, 37: 481−488.

[36] SONG Y, ZHANG S, LI J, ZHAO C, ZHANG X. Electrodeposition of Ca−P coatings on biodegradable Mg alloy: In vitro biomineralization behavior [J]. Acta Biomater, 2010; 6: 1736−1742.

[37] KAHRIZSANGI R E, TABRIZI B N, CHAMI A. Synthesis and characteri- zation of fluorapatiteetitania (FAp−TiO_2) nanocomposite via mechanochemical process [J]. Solid State Sci, 2010, 12: 1645−1651.

[38] ZAHRANI E M, FATHI M H. The effect of high-energy ball milling parameters on the preparation and characterization of fluorapatite nanocrystalline powder [J]. Ceram Int, 2009, 35: 2311−2323.

[39] PARK J H, LEE D Y, OH K T, LEE Y K. Bioactivity of calcium phosphate coatings prepared by electrodeposition in a modified simulated body fluid [J]. Mater Lett, 2006, 60: 2573−2577.

[40] BAKHSHESHI-RAD H R, IDRIS M H M H, KADIR M R A, DAROONPARVAR M. Effect of fluoride treatment on corrosion behavior of Mg−Ca binary alloy for implant application [J]. Transactions of Nonferrous Metals Society of China, 2013, 23: 699−710.

[41] TOMOZAWA M, HIROMOTO S. Microstructure of hydroxyapatite and octacalcium phosphate-coatings formed on magnesium by a hydrothermal treatment at various pH values [J]. Acta Mater, 2011, 59: 355−363.

[42] ZHANG J M, LIN C J, FENG Z D, TIAN Z W. Mechanistic studies of electrodeposition for bioceramic coatings of calcium phosphates by an in situ pH-microsensor technique [J]. J Electroanal Chem, 1998, 452: 235−240.

[43] ZHOU W, SHAN D, HAN E H, KE W. Structure and formation mechanism of phosphate conversion coating on die-cast AZ91D magnesium alloy [J]. Corros Sci, 2008, 50: 329−337.

[44] GU X N, LI N, ZHOU W R, ZHENG Y F, ZHAO X. Corrosion resistance and surface biocompatibility of a micro arc oxidation coating on a Mg−Ca alloy [J]. Acta Biomater, 2011, 7: 1880−1889.

[45] BAKHSHESHI-RAD H R, ABDUL-KADIR M R, IDRIS M H, FARAHANY S. Relationship between the corrosion behavior and the thermal characteristics and microstructure of Mg−0.5Ca−xZn alloys [J]. Corros Sci, 2012, 64: 184−197.

[46] BOSE S, DASGUPTA S, TARAFDER S, BANDYOPADHYAY A. Microwave-processed nanocrystalline hydroxyapatite: Simultaneous enhancement of mechanical and biological properties [J]. Acta Biomater, 2010, 6: 3782−3790.

[47] GU Y, BANDOPADHYAY S, CHEN C, NING C, GUO Y. Long-term corrosion inhibition mechanism of microarc oxidation coated AZ31 Mg alloys for biomedical applications [J]. Mater Design, 2013, 46: 66−75.

表面涂覆含氟羟基磷灰石和缺钙羟基磷灰石的镁合金体外降解行为

H. R. BAKHSHESHI-RAD[1], E. HAMZAH[1], M. DAROONPARVAR[1],
M. A. M. YAJID[1], M. KASIRI-ASGARANI[2], M. R. ABDUL-KADIR[1], M. MEDRAJ[3]

1. Department of Materials, Manufacturing and Industrial Engineering, Faculty of Mechanical Engineering,
Universiti Teknologi Malaysia, 81310 Johor Bahru, Johor, Malaysia;
2. Materials Engineering Department, Najafabad Branch, Islamic Azad University, Najafabad, Isfahan, Iran;
3. Department of Mechanical Engineering, Concordia University, 1455 De Maisonneuve Blvd. West,
Montreal, QC H3G 1M8, Canada

摘　要：通过电化学沉积方法，在生物降解镁合金表面覆盖含氟羟基磷灰石(FHA)涂层和缺钙羟基磷灰石(CDHA)涂层。采用 X 射线衍射、傅立叶变换红外光谱、透射电子显微镜、扫描电子显微镜和能量色散 X 射线光谱研究涂层特性。结果表明：涂覆纳米 FHA 涂层的样品具有垂直于样品表面的纳米针状结构，比涂覆 CDHA 涂层样品的结构更致密和更均匀。纳米 FHA 涂层比纳米 CDHA 涂层具有更小的晶粒尺寸，分别为 65 nm 和 95 nm。然而，CDHA 涂层比 FHA 涂层更厚，厚度分别为 19 μm 和 15 μm。通过极化、浸泡和析氢实验研究的腐蚀行为表明：纳米 FHA 涂层和纳米 CDHA 涂层显著降低腐蚀速率并引起钝化。纳米 FHA 和纳米 CDHA 涂层可以加速骨状磷灰石层的形成，相比未覆盖的镁合金可以显著减少溶出速率。纳米 FHA 涂层能对镁合金提供有效的防护并具有更高的腐蚀性能。因此，覆盖纳米 FHA 涂层的镁合金在整形外科领域具有良好的应用前景。

关键词：镁合金；含氟羟基磷灰石；缺钙羟基磷灰石；电沉积；腐蚀行为

(Edited by Chao WANG)